

# Polynomial Preconditioners for Regularized Linear Inverse Problems <sup>\*</sup>

Siddharth S. Iyer<sup>†</sup>, Frank Ong<sup>‡</sup>, Xiaozhi Cao<sup>§</sup>, Congyu Liao<sup>§</sup>, Luca Daniel<sup>†</sup>, Jonathan I. Tamir<sup>\*¶</sup>, and Kawin Setsompop<sup>\*‡§</sup>

**Abstract.** This work aims to accelerate the convergence of proximal gradient methods used to solve regularized linear inverse problems. This is achieved by designing a polynomial-based preconditioner that targets the eigenvalue spectrum of the normal operator derived from the linear operator. The preconditioner does not assume any explicit structure on the linear function and thus can be deployed in diverse applications of interest. The efficacy of the preconditioner is validated on three different Magnetic Resonance Imaging applications, where it is seen to achieve faster iterative convergence while achieving similar reconstruction quality.

**Key words.** regularized linear inverse problems, polynomial preconditioner, proximal gradient descent

**MSC codes.** 90C06, 90C90, 90C25, 92C55

**1. Introduction.** Linear inverse problems, particularly those derived from compressed sensing formulations, are typically posed as the following optimization problem [15, 10]:

$$(1.1) \quad x^* = \begin{cases} \operatorname{argmin}_x & g(x) \\ \text{subject to} & Ax = b \end{cases}$$

Here,  $A : \mathbb{C}^n \rightarrow \mathbb{C}^m$  is the linear forward model or the measurement matrix,  $b \in \mathbb{C}^m$  is the acquired data or measurement vector and  $g : \mathbb{C}^n \rightarrow \mathbb{R}$  is a prior regularization function, often the  $l_1$ -norm, to enforce sparsity. In practice, due to measurement errors (such as noise), the following optimization problem is solved instead [15, 26, 4, 25, 13]:

$$(1.2) \quad x^* = \begin{cases} \operatorname{argmin}_x & g(x) \\ \text{subject to} & \|Ax - b\|_2 \leq \epsilon \end{cases}$$

<sup>\*</sup>Submitted to the editors September 27, 2022.

**Funding:** This work was supported in part by the National Institute of Health under Grants R01EB020613, R01MH116173, R01EB019437, U01EB025162, and P41EB030006, and in part by GE Healthcare.

<sup>†</sup>Department of Electrical Engineering and Computer Science, Massachusetts Institute of Technology, Cambridge, MA (ssi.compens@gmail.com, dluca@mit.edu).

<sup>‡</sup>Department of Electrical Engineering, Stanford University, Stanford, CA (frankongh@gmail.com, kawins@stanford.edu).

<sup>§</sup>Department of Radiology, Stanford University, Stanford, CA (xiaozhic@stanford.edu, cyliao@stanford.edu).

<sup>¶</sup>Departments of Electrical and Computer Engineering, Diagnostic Medicine, and Oden Institute, University of Texas at Austin, Austin, TX (jtamir@utexas.edu).

<sup>\*</sup>J. I. Tamir and K. Setsompop contributed equally to this article.

Parts of this work have been presented at the ISMRM Annual Conference of 2022 [18].

The optimization (1.2) is often re-cast as the following unconstrained problem for ease-of-computation:

$$(1.3) \quad x^* = \left\{ \underset{x}{\operatorname{argmin}} \quad \frac{1}{2} \|Ax - b\|_2^2 + \lambda g(x) \right.$$

The Karush-Kuhn-Tucker (KKT) conditions can be used to verify that for any  $\epsilon$ , there is an appropriate choice of  $\lambda$  such that the solutions of (1.2) and (1.3) coincide.

The unconstrained formulation (1.3) is commonly utilized for solving ill-conditioned least squares problems, where the regularization ( $g$ ) helps stabilize the solution. When  $g$  is the  $l_1$ -norm, the unconstrained formulation (1.3) is commonly called referred to as ‘‘LASSO’’ [47].

**1.1. Motivation.** In computational Magnetic Resonance Imaging (MRI), iterative proximal methods [37] have emerged as the workhorse algorithms to solve linear inverse problems that are posed in the form of (1.3) [26, 27, 4, 25, 13]. This is arguably because:

1. These algorithms are highly generalizable as they do not impose any restrictions on the utilized regularization function ( $g$ ) (as long as the proximal operator of ( $g$ ), defined in the sequel, can be calculated).
2. These algorithms leverage matrix-free implementations of the forward-model  $A$  (i.e., the individual coordinates or entries of  $A$  are not known or stored in memory) for computationally efficient processing of high-dimensional problems.

Due to the above mentioned advantages, MRI reconstructions are typically posed as (1.3) and are solved using the Fast Iterative Shrinkage-Thresholding Algorithm (FISTA)[2], which enjoys theoretically optimal convergence. However, the iterative convergence of FISTA and other iterative proximal methods is largely limited by the conditioning of  $A$  as determined by the eigenvalues of  $A^*A$ , where  $A^*$  is the adjoint of  $A$ . This limits the integration of MRI applications with an ill-posed  $A$  that leverage (1.3) into clinical practice, as the ill-conditioning results in long reconstruction times.

**1.2. Contributions.** This work proposes a generalizable polynomial-based preconditioner for faster iterative convergence of regularized linear inverse problems that leverage proximal gradient methods (like FISTA). The evolution of the iterates in proximal gradient descent (PGD) [37] is analyzed and a cost function for polynomial optimization is derived such that the optimized polynomial ( $p$ ), when utilized as a spectral function, directly improves the convergence rate of PGD (and subsequently, FISTA). The proposed preconditioner  $P$  is evaluated as  $P = p(A^*A)$ . Once the polynomial is calculated, it can be applied to any application with forward model  $A$  as long as the maximum eigenvalue of  $A^*A$  can be estimated. (Note that standard FISTA also requires an estimate of the maximum eigenvalue of  $A^*A$ .) The proposed preconditioner does not assume any structure on  $A$ , and can leverage matrix-free implementations of  $A^*A$ . Similarly, the proposed preconditioner does not assume any additional structure on  $g$  other than that its proximal operator, defined in the sequel, can be evaluated. Thus, the proposed preconditioner is highly generalizable and can be applied to various regularized linear inverse problems of interest. In particular, the proposed method retains the ‘‘plug-and-play’’ property of FISTA, and is thus an ideal candidate for integration into reconstruction toolboxes like SigPy [35], MIRT [12] and BART [49] whose users typically leverage proximal algorithms in an ‘‘out-of-the-box’’ manner.

**1.3. Related Works.** A polynomial-based preconditioner for accelerating FISTA, which will be denoted “IFISTA” in this work, was presented in [60]. IFISTA uses a polynomial with binomial coefficients to construct the preconditioner by evaluating the polynomial on  $A^*A$ . In contrast, the polynomial coefficients used in this work are obtained from optimizing a cost function derived from analyzing the error propagation over iterations of PGD which, for a fixed polynomial degree, results in polynomial coefficients that more explicitly target the improved convergence compared to the binomial coefficients used in IFISTA. In fact, the cost function utilized in this work has a natural connection to [19], where a similar cost function was proposed as a means of accelerating the convergence of the Conjugate Gradient. While [19] focuses explicitly on ordinary least squares without regularization and motivates the polynomial design as a means of approximating the inverse of  $A^*A$ , this work arrives at the same cost function for polynomial design, but from the completely different perspective of using PGD to solve ill-posed problems that leverage regularization.

Jacobi-like “left-preconditioning” methods have also been proposed as a means of accelerating convergence, where a matrix  $D$  is designed so that  $A^*DA$  is better conditioned.  $D$  is then incorporated into the least-squares cost in (1.3) to yield the following [36]:

$$(1.4) \quad x^* = \left\{ \underset{x}{\operatorname{argmin}} \quad \frac{1}{2} \|D^{1/2}(Ax - b)\|_2^2 + \lambda g(x) \right.$$

For non-Cartesian MRI, these methods are typically called “Density Compensation” and have seen wide adoption [39, 40]. Note that by defining  $A_{\text{DCF}}$  and  $b_{\text{DCF}}$  as  $D^{1/2}A$  and  $D^{1/2}b$  respectively, (1.4) is a special case of (1.3). Thus, general methods like FISTA, IFISTA and the proposed preconditioner can synergistically leverage such structure-based left-preconditioning.

In the intersection of computational MRI and regularized linear inverse problems, several preconditioning methods have been proposed that leverage the circulant structure of  $A$ , such as in [23, 42, 55, 31]. In [36], a Frobenius-norm-optimized diagonal preconditioner for the dual variables of the primal-dual hybrid gradient (PDHG) algorithm [8] was presented to improve convergence for non-Cartesian MRI applications. However, by utilizing explicit structure, it is unclear on whether the mentioned methods will generalize well to an arbitrary  $A$ . This increases the barriers to entry of such preconditioning methods, particularly for novel applications. This is particularly true for recent contrast-resolved MRI applications [6, 46, 54, 28, 24, 17, 58, 52, 3, 21, 51, 5] with large measurement sizes and an ill-conditioned forward operator  $A$  such as Echo Planar Time Resolved Imaging [54] and Magnetic Resonance Fingerprinting (MRF) [28, 5, 6]. The high dimensionality and ill-conditioning of  $A$  may also result in computationally intensive procedures to estimate the preconditioner, such as with the Frobenius norm formulation used in [36] and circulant preconditioner design process proposed in [31].

Another advantage of FISTA, IFISTA and the proposed preconditioner is that they can utilize efficient implementations of the normal operator ( $A^*A$ ), which cannot be leveraged by PDHG and [36]. For example, non-Cartesian MRI reconstructions can leverage the Toeplitz structure of the normal operator of the non-uniform Fourier transform to avoid expensive gridding operations [53, 14, 1]. Temporal subspace methods such as  $T_2$ -Shuffling can use the “spatio-temporal” kernel to avoid expanding into the “echo” dimension at each iteration to significantly reduce the number of Fast Fourier Transforms needed [46].

In applications where the regularization ( $g$ ) is cognate to the  $l_1$ -norm to enforce sparsity, algorithms that accelerate Iteratively Re-Weighted Least Squares (IRWLS) [11, 15] have been proposed such as [56] and [9]. However, since these algorithms do not use proximal operators, it limits the different types of regularizations that can be tested without significantly modifying the chosen algorithm. For example, should a user choose to use the algorithm proposed in [9], it is on the user to verify whether their operator  $A$  is “diagonally dominant” and that their chosen regularization ( $g$ ) yields an easy-to-calculate preconditioner (which is re-calculated at every outer iteration).

In the spirit of generalizability and to retain the simplicity and the “plug-an-play” benefits of FISTA, this work compares and contrasts the iterative convergence of the proposed preconditioner against other generalizable methods like FISTA, IFISTA and the Alternating Direction Method of Multipliers (ADMM) [37].

**2. Theory.** Without loss of generality, let the induced norm of  $A$  be unitary, which then implies the eigenvalues of  $A^*A$  and  $AA^*$  lie in the interval  $[0, 1]$ . Let  $\langle \cdot, \cdot \rangle$  denote the standard Euclidean complex inner product, and let  $\|\cdot\|_p$  denote the standard Euclidean  $l_p$ -norm.

The sequel will focus on the unconstrained formulation (1.3) as the experiments leverage the smoothness of the least squares term in the objective function for faster convergence via Nesterov acceleration [2, 32].

*Remark 2.1.* For simplicity, the following analysis focuses on traditional PGD. That being said, the improved conditioning of the method naturally translates into faster convergence when using FISTA as well.

**2.1. Background.** Following [37], the proximal operator of a closed and proper convex function  $g$  is defined as:

**Definition 2.2 (Proximal Operator).**

$$(2.1) \quad \mathbf{prox}_{\alpha g}(v) = \left\{ \underset{x}{\operatorname{argmin}} \quad \frac{1}{2} \|x - v\|_2^2 + \alpha g(x) \right.$$

This proximal operator is used in the Proximal Gradient Descent (PGD) algorithm to solve optimization algorithms of the form (1.3) [37]. With the assumption that the induced norm of  $A$  is unitary, the PGD algorithm to solve (1.3) is listed as Algorithm 2.1.

---

**Algorithm 2.1** Proximal Gradient Descent [37]

---

*Inputs:*

- forward model  $A$
- measurements  $b$
- proximal operator  $\mathbf{prox}_{\lambda g}$
- $x_0 = 0$

*Step  $k$ :* ( $k \geq 0$ ) Compute

$$(2.2) \quad x_{k+1} = \mathbf{prox}_{\lambda g}(x_k - A^*(Ax_k - b))$$


---

The iterations of Algorithm 2.1 converge to the optimal solution of (1.3), denoted  $x^*$ , which is a stationary point.

**Theorem 2.3 (Fixed Point Property of PGD [37]).** *A solution  $x^*$  is the optimal solution to (1.3) if and only if*

$$(2.3) \quad x^* = \mathbf{prox}_{\lambda g}(x^* - A^*(Ax^* - b))$$

Assuming  $\mathbf{prox}_{\lambda g}$  has a closed form or easy-to-implement solution, PGD is a robust and simple-to-implement algorithm that achieves  $O(1/k)$  iterative convergence [2]. To improve the iterative convergence, FISTA [2] was proposed that achieves  $O(1/k^2)$  iterative convergence by smartly choosing different point  $z_k$  (instead of  $x_k$ ) to evaluate (2.2). Listed as Algorithm 2.2 is the FISTA algorithm that utilizes  $\beta_k$  proposed in [7] to solve (1.3).

---

**Algorithm 2.2** FISTA[2] with  $\beta_k$  from [7]

---

*Inputs:*

- forward model  $A$
- measurements  $b$
- proximal operator  $\mathbf{prox}_{\lambda g}$
- $x_{-1} = x_0 = 0$

*Step  $k$ :* ( $k \geq 0$ ) Compute

$$(2.4a) \quad x_{k+1} = \mathbf{prox}_{\lambda g}(z_k - A^*(Az_k - b))$$

$$(2.4b) \quad \beta_k = k/(k+3)$$

$$(2.4c) \quad z_{k+1} = x_k + \beta_k(x_k - x_{k-1})$$


---

A useful property of proximal operators that will be utilized in the sequel is the *firm non-expansiveness* property.

**Lemma 2.4 (Firm Non-Expansiveness Property [37]).** *For all  $x, y \in \mathbb{C}^n$ ,*

$$(2.5) \quad \|\mathbf{prox}_{\lambda g}(x) - \mathbf{prox}_{\lambda g}(y)\|_2 \leq \|x - y\|_2$$

**2.2. Slow Convergence of PGD.** Lemma 2.4 helps illustrate how the convergence of iterates of PGD is affected by the eigenvalue spectrum of  $A$ .

**Theorem 2.5.** *The error of iterates  $x_k$  in Algorithm 2.1 with respect to  $x^*$  are upper-bounded by the spectrum of  $(I - A^*A)$ .*

*Proof.* Let  $e_k = x_k - x^*$  be the error over iterations. Subtracting (2.2) with (2.3), taking the  $l_2$ -norm and utilizing Lemma 2.4 yields:

$$(2.6) \quad \|e_{k+1}\|_2 \leq \|(I - A^*A)e_k\|_2$$

In particular, splitting  $e_k$  into  $s_k + t_k$  where  $s_k \in \text{null}(A)$  and  $t_k \in \text{null}(A)^\perp$  results in:

$$(2.7) \quad \|e_{k+1}\|_2^2 \leq \|(I - A^*A)t_k\|_2^2 + \|s_k\|_2^2 \quad \blacksquare$$

Therefore, the decrease in error of  $e_k$  within  $\text{null}(A)^\perp$  (i.e.  $t_k$ ) is upper-bounded by the eigenvalue spectrum of  $I - A^*A$ . This bound is strict when  $A^*A$  is injective.

**Corollary 2.6.** *If  $A^*A$  has no zero valued eigenvalues, the inequality in (2.6) is strict.*

Thus, inverse problems involving an  $A^*A$  with small eigenvalues may suffer from slow iterative convergence.

**2.3. Main Results.** Theorem 2.5 motivates the design of a preconditioner that minimizes the magnitude of the eigenvalues of  $I - A^*A$  for faster convergence. The main result of this work is to modify the gradient update steps in Algorithm 2.1 and Algorithm 2.2 using preconditioner  $P = p(A^*A)$ , where  $p$  is designed in such a way that  $p(A^*A)$  increases the contributions of the smaller eigenvalues of  $A^*A$  over iterations for faster convergence.

Let  $p$  have fixed degree  $d$ , where  $d$  is a hyper-parameter that is to be tuned for the application of interest. The coefficients of  $p$  are calculated by optimizing over (2.8), which is motivated in Subsection 2.5.

$$(2.8) \quad p = \left\{ \underset{q}{\operatorname{argmin}} \int_{z=0}^1 (1 - q(z)z)^2 dz \right.$$

The polynomial from (2.8) is then used to derive preconditioner  $p(A^*A)$  that is included in Algorithm 2.1 to arrive at Algorithm 2.3. The derivation is in Subsection 2.4.

---

**Algorithm 2.3** Polynomial Preconditioning for PGD

---

*Inputs:*

- forward model  $A$
- measurements  $b$
- proximal operator  $\mathbf{prox}_{\lambda g}$
- optimized polynomial  $p$  from (2.8)
- $y_0 = 0$ .

*Step  $k$ :* ( $k \geq 0$ ) Compute

$$(2.9) \quad y_{k+1} = \mathbf{prox}_{\lambda g}(y_k - p(A^*A)A^*(Ay_k - b))$$


---

*Remark 2.7.* The iteration variable name has been changed in Algorithm 2.3 (and the following Algorithm 2.4) from  $x_k$  to  $y_k$  to emphasize that the preconditioner is being used.

Similarly, the preconditioner is integrated into Algorithm 2.2 to arrive at Algorithm 2.4.

**2.4. Deriving Polynomial Preconditioning for PGD.** It helps to derive Algorithm 2.3 before discussing (2.8). To motivate Algorithm 2.3, first consider the exact formulation (1.1) with  $b \in \text{range}(A)$ . Let the singular value decomposition (SVD) of  $A$  in dyadic form be as follows:

$$(2.11) \quad A(\cdot) = \sum_{i=1}^j \sigma_i \langle \cdot, v_i \rangle u_i$$

**Algorithm 2.4** Polynomial Preconditioning for FISTA*Inputs:*

- forward model  $A$
- measurements  $b$
- proximal operator  $\mathbf{prox}_{\lambda g}$
- optimized polynomial  $p$  from (2.8)
- $y_{-1} = y_0 = 0$ .

*Step  $k$ :* ( $k \geq 0$ ) Compute

$$(2.10a) \quad y_{k+1} = \mathbf{prox}_{\lambda g}(z_k - p(A^*A)A^*(Az_k - b))$$

$$(2.10b) \quad \beta_k = k/(k+3)$$

$$(2.10c) \quad z_{k+1} = y_k + \beta_k(y_k - y_{k-1})$$

Here,  $j \leq n$ ,  $1 \geq \sigma_1 \geq \sigma_2 \geq \dots \geq \sigma_j > 0$  are the singular values of  $A$ ,  $\{u_i\}$  and  $\{v_i\}$  are the left and right singular vectors respectively, and Let  $p(z)$  be a polynomial of degree  $d$  such that  $p(z) > 0$  for  $z \in (0, 1]$ , and let  $P = p(AA^*)$ .

$$(2.12) \quad P(\cdot) = \sum_{i=1}^j p(\sigma_i^2) \langle \cdot, u_i \rangle u_i$$

As an ansatz, let  $P^{\frac{1}{2}}$  be the square root of  $P$ :

$$(2.13) \quad P^{\frac{1}{2}}(\cdot) = \sum_{i=1}^j [p(\sigma_i^2)]^{\frac{1}{2}} \langle \cdot, u_i \rangle u_i$$

**Lemma 2.8.** *The condition  $Ax = b$  in (1.1) is equivalently enforced by the constraint  $P^{\frac{1}{2}}Ax = P^{\frac{1}{2}}b$ .*

*Proof.* The condition  $p(z) > 0$  for  $z \in (0, 1]$  implies  $P$  and  $P^{\frac{1}{2}}$  are injective when the domain and co-domain for both operators are restricted to  $\text{range}(A)$ . ■

Lemma 2.8 motivates the following “preconditioned” formulation that has the same solution as (1.1).

$$(2.14) \quad x^* = \begin{cases} \underset{x}{\operatorname{argmin}} & g(x) \\ \text{subject to} & P^{\frac{1}{2}}Ax = P^{\frac{1}{2}}b \end{cases}$$

To account for model and measurement errors, (2.14) is relaxed to the following constrained formulation:

$$(2.15) \quad x^* = \begin{cases} \underset{x}{\operatorname{argmin}} & g(x) \\ \text{subject to} & \|P^{\frac{1}{2}}(Ax - b)\|_2 \leq \epsilon_p \end{cases}$$

Note that  $\epsilon$  and  $\epsilon_p$  in the constraints of (1.2) and (2.15) respectively are likely to be different as  $P^{\frac{1}{2}}$  is not necessarily unitary.

Similarly to how (1.2) is recast to (1.3), (2.15) is solved by the following for an appropriate choice of  $\lambda_p$ .

$$(2.16) \quad x^* = \left\{ \operatorname{argmin}_x \frac{1}{2} \|P^{\frac{1}{2}}(Ax - b)\|_2^2 + \lambda_p g(x) \right.$$

Defining  $A_P = P^{\frac{1}{2}}A$  and  $b_P = P^{\frac{1}{2}}b$ , the PGD iterations to solve (2.16) and the fixed point condition (Theorem 2.3) of (2.16) is as follows:

$$(2.17a) \quad y_{k+1} = \operatorname{prox}_{\lambda_p g}(y_k - A_P^*(A_P y_k - b_P))$$

$$(2.17b) \quad y^* = \operatorname{prox}_{\lambda_p g}(y^* - A_P^*(A_P y^* - b_P))$$

Here,  $y^*$  is the solution to (2.16).

To significantly simplify the iterations of (2.17), the permutability of spectral functions and  $A^*A$ , listed as Lemma 2.9, is leveraged.

**Lemma 2.9 (Permutability of Spectral Functions).**

$$(2.18a) \quad A^*p(AA^*)A = p(A^*A)A^*A$$

$$(2.18b) \quad A^*p(AA^*) = p(A^*A)A^*$$

*Proof.* Since  $p$  is a spectral function of  $A$ ,  $p(AA^*)$  and  $p(A^*A)$  can be evaluated with respect to the singular value decomposition of  $A$  as defined in (2.11) and (2.12) to verify this result. ■

Incorporating Lemma 2.9 into (2.17) results in:

$$(2.19a) \quad y_{k+1} = \operatorname{prox}_{\lambda_p g}(y_k - p(A^*A)A^*(Ay_k - b))$$

$$(2.19b) \quad y^* = \operatorname{prox}_{\lambda_p g}(y^* - p(A^*A)A^*(Ay^* - b))$$

This yields the Algorithm 2.3.

*Remark 2.10.* Solving (2.16) with FISTA and using Lemma 2.9 results in Algorithm 2.4.

**2.5. Polynomial Design.** A line of reasoning similar to Theorem 2.5 is used to arrive at (2.8).

**Theorem 2.11.** *The error of iterates  $y_k$  in Algorithm 2.3 with respect to  $y^*$  are upper-bounded by the spectrum of  $(I - p(A^*A)A^*A)$ .*

*Proof.* Let  $e_k = y_k - y^*$  be the error over iterations. Subtracting the equations of (2.19), taking the  $l_2$ -norm and utilizing Lemma 2.4 yields:

$$(2.20) \quad \|e_{k+1}\|_2 \leq \|(I - p(A^*A)A^*A)e_k\|_2$$

Similarly to Theorem 2.5, splitting  $e_k$  into  $s_k + t_k$  where  $s_k \in \operatorname{null}(A)$  and  $t_k \in \operatorname{null}(A)^\perp$  results in:

$$(2.21) \quad \|e_{k+1}\|_2^2 \leq \|(I - p(A^*A)A^*A)t_k\|_2^2 + \|s_k\|_2^2 \quad \blacksquare$$



Theorem 2.11 motivates finding a polynomial  $p$  such that  $I - p(A^*A)A^*A$  is as close to zero as possible. As the dimensions of  $A$  are typically very large, it is not computationally feasible (in terms of processing time) to perform an eigenvalue decomposition of  $A^*A$  to use as prior information for polynomial design. To avoid this, the coefficients of the polynomial  $p$  is found by optimizing the continuous approximation of the induced norm. This is listed as (2.8). The polynomial that minimizes (2.8) in-turn minimizes the induced  $l_2$ -norm of  $I - p(A^*A)A^*A$  in Theorem 2.11.

In other words, the component  $t_k$  in  $v_i$  (as in (2.21) and (2.11)) is upper-bounded by  $|1 - p(\sigma_i^2)\sigma_i^2|$ , which according to (2.8), is minimized to be close to zero. Note that the larger degree  $d$  of polynomial  $p$ , the better  $(1 - p(x)x)^2$  (equivalently  $|1 - p(x)x|$ ), can approximate the zero function.

Priors on the spectrum can be easily incorporated into (2.8) as follows:

$$(2.22) \quad p = \left\{ \operatorname{argmin}_q \int_{z=0}^1 w(z)(1 - q(z)z)^2 dz \right.$$

Here,  $w$  can weight the cost to prioritize certain components of the spectrum.

*Remark 2.12.* At first glance, minimizing the following objective instead of (2.8) is preferable as it directly translates into minimizing the appropriate induced norm of Theorem 2.11:

$$(2.23) \quad p = \left\{ \operatorname{argmin}_q \max_{z \in (0,1]} |1 - q(z)z| \right.$$

It is well known that Chebyshev polynomials of the first kind can be used to derive the optimal polynomials such that the maximum absolute value of that polynomial over a specified interval is minimized. However, defining  $r(z) = 1 - q(z)z$ , and using Chebyshev polynomials to determine  $r$  yields a polynomial with  $r(z) = 1$  for multiple values of  $z \in [0, 1]$  due to the constraint  $r(0) = 1$ , which implies the components of  $t_k$  in (2.21) corresponding to eigenvalues  $\sigma^2$  such that  $r(\sigma^2) = 1$  will not decrease. However, if the minimum non-zero eigenvalue  $\mu = \sigma_j^2$  of  $A^*A$  is known a-priori, the following polynomial minimizes (2.23) over the interval  $[\mu, 1]$  (See [44, 20, 50, 19]):

$$(2.24a) \quad r(z) = \frac{T_{d+1}\left(\frac{1+\mu-2z}{1-\mu}\right)}{T_{d+1}\left(\frac{1+\mu}{1-\mu}\right)}$$

$$(2.24b) \quad p(z) = \frac{1 - r(z)}{z}$$

Here,  $T_{d+1}$  is the Chebyshev polynomial of the first kind of degree  $d + 1$ . In practice, (2.8) is preferred as it is often computationally expensive to estimate  $\mu$  unless  $A^*A$  happens to be injective, in which case  $\mu$  can be estimated by performing power-iteration on  $I - A^*A$ .

*Remark 2.13.* Rather interestingly, while (2.8) and (2.23) were motivated by studying the evolution of iterates in PGD when solving regularized linear inverse problems in the form of (1.3), the exact formulation for polynomial optimization was studied in [19] as a means of accelerating the convergence of Conjugate Gradient for ordinary least squares optimization,

where (2.8) and (2.23) were optimized to construct an incomplete inverse of  $(A^*A)$  to use a preconditioner.

Theorem 2.14 verifies that the positivity assumption in Lemma 2.8 is satisfied by optimized results of (2.8) and (2.23).

**Theorem 2.14 (Polynomial Positivity).** *The polynomial  $p$  derived from optimized (2.8) and (2.23) satisfies the constraint  $p(z) > 0$  for  $z \in (0, 1]$ .*

*Proof.* This is a consequence of Theorem 4 of [19]. ■

**2.6. Error Bound.** With the simplifying assumptions that  $A^*A$  is injective and  $\lambda_p = \lambda$ , Theorem 2.15 bounds the difference between the solutions of (1.3) and (2.16). Let  $\|\cdot\|_{2 \rightarrow 2}$  denote the induced  $l_2$ -norm.

**Theorem 2.15.** *Assume  $A^*A$  is injective, and  $\lambda = \lambda_p$  in (1.3) and (2.16) respectively. Let  $e_k, \gamma$  and  $\delta$  be defined as:*

$$(2.25a) \quad e_k = y_k - x^*$$

$$(2.25b) \quad \gamma = \|I - p(A^*A)A^*A\|_{2 \rightarrow 2}$$

$$(2.25c) \quad \delta = \|(I - p(A^*A))A^*(Ax^* - b)\|_2$$

Here,  $x^*$  is the optimal solution to (1.3),  $y_k$  are the iterates of Algorithm 2.3 that leverages polynomial  $p$ . Then, the limit of the difference,  $e_\infty$ , satisfies the following:

$$(2.26) \quad \|e_\infty\|_2 \leq \frac{\delta}{1 - \gamma}$$

*Proof.* Subtracting (2.9) from (2.3), taking the  $l_2$ -norm of the difference and utilizing Lemma 2.4 with the triangle inequality yields:

$$(2.27) \quad \|e_{k+1}\|_2 \leq \|(I - PA^*A)e_k\|_2 + \|(I - P)A^*(Ax^* - b)\|_2$$

This reduces to:

$$(2.28) \quad \|e_{k+1}\|_2 \leq \gamma \|e_k\|_2 + \delta$$

As  $A^*A$  is injective, it follows that, after optimizing for  $P$  via (2.8) or (2.23),  $\gamma < 1$ . This in-turn implies (2.28) converges and the limit  $e_\infty$  satisfies (2.26). ■

For most regularized linear inverse problems,  $\|Ax^* - b\|$  is small, which in turn implies the error between (1.3) and (2.16) is also small as:

$$(2.29) \quad \delta \leq \|I - p(A^*A)\|_{2 \rightarrow 2} \|A^*(Ax^* - b)\|_2$$

**2.7. Implementation Details and Complexity Analysis.** Prior works [19, 60] that used polynomial preconditioning utilized the matrix entries of  $A$  to explicitly pre-calculate  $p(A^*A)$  to save computation time. Since this work aims to leverage matrix-free implementations of  $A$ , this is no longer possible. Rather, utilizing a polynomial preconditioner of degree  $d$  involves  $(d + 1)$   $A^*A$  evaluations per iteration, thereby increasing the per-iteration cost compared to

PGD and FISTA. However, the main benefit of the preconditioner is that, for the same number of  $A^*A$  evaluations, the components of the iterates corresponding to the smaller eigenvalues of  $A^*A$  are more explicitly targeted. To make sure this point is well reflected in the sequel, the experiments in Section 3 reports convergence as a function of the total number of  $A^*A$  evaluations (and the number of iterations, which reflects the number of proximal operator evaluations) in addition to reporting the iterative convergence as a function of wall time to demonstrate real world performance.

To give an example, Figure 1 depicts the iteration progress assuming a degree 3 polynomial optimized using (2.8) after 4  $A^*A$  evaluations for Algorithm 2.1 and Algorithm 2.3, which shows that the polynomial preconditioner aids the convergence of components corresponding to the lower eigenvalues of  $A^*A$  at the cost of slightly slower convergence of the higher eigenvalues. In the sequel, the degree of the polynomial is a hyper-parameter that is tuned for the application of interest.

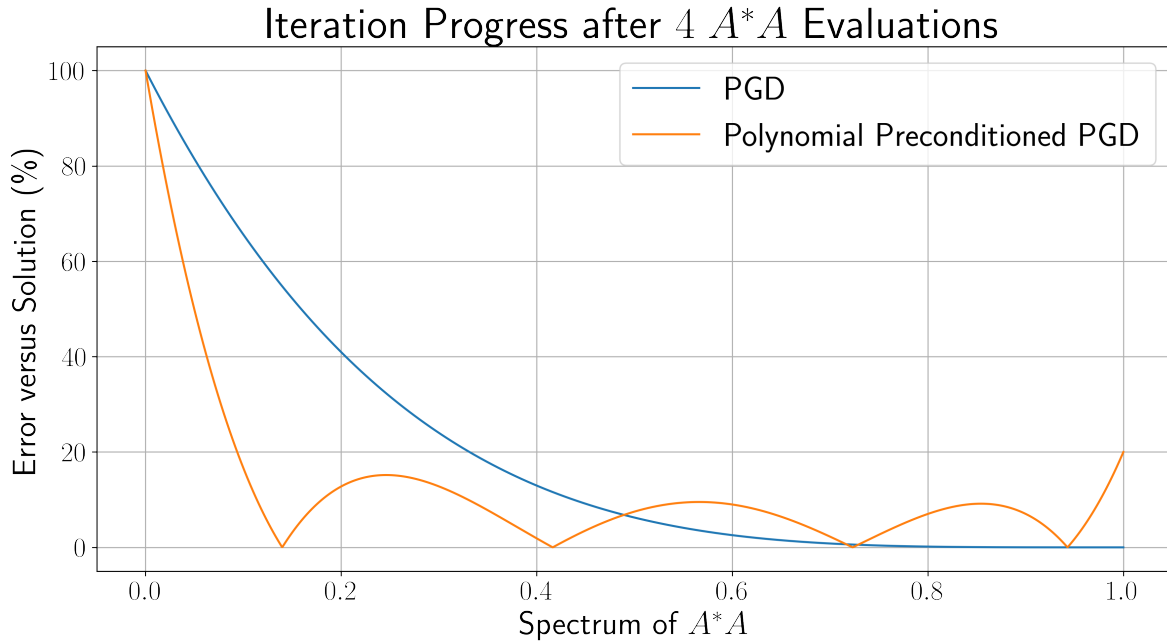


**Figure 1.** Iteration progress of Algorithm 2.1 and Algorithm 2.3 assuming a degree 3 polynomial optimized using (2.8) after  $4A^*A$  evaluations. The  $x$ -axis denotes the spectrum of  $A^*A$ . The  $y$ -axis denotes the percentage of decrease of error with respect to the respective final iterates. This figure shows that the polynomial preconditioner aids the convergence of components corresponding to the lower eigenvalues of  $A^*A$  at the cost of slower convergence of the higher eigenvalues.

*Remark 2.16.* Note that for both, numerical stability and achieving  $(d+1)$  evaluations of  $A^*A$  per iteration, it is important to leverage the polynomial structure when evaluating the preconditioner. For example, consider pseudo-code implementation in Listing 1 that utilizes recursion. It is assumed that “ListofPolynomialCoefficients” returns the coefficients of  $p$  in

## Listing 1

Pseudo-code for Polynomial Evaluation

```

I = IdentityOperator ()
N = ForwardModelNormalOperator ()

def CreatePolynomialPreconditioner (c):
    if len(c) == 1:
        return c[0] * I
    else:
        return c[0] * I + N * CreatePolynomialPreconditioner (c[1:])

coeffs = ListOfPolynomialCoefficients ()
Preconditioner = CreatePolynomialPreconditioner (coeffs)

```

the order:

$$(2.30) \quad p(x) = \sum_{i=0}^d c[i]x^i$$

**2.8. Interpretation and Noise Coloring.** At first glance, the proposed preconditioner is similar to the left-preconditioning methods such as (1.4). However, instead of using a diagonal matrix to weight to the entries (or coordinates) of the measurement  $b$ ,  $P^{1/2}$  “spectrally” weights  $b$ . In other words,  $P^{1/2}$  is a diagonal matrix with respect to the left singular vectors of  $A$  (or  $\{u_i\}$ ). A unique consequence of this property is that, in the absence of regularization, polynomial preconditioning result in the same solution as (1.3) and thus introduces no noise coloring. This is not necessarily true for general left-preconditioning methods.

**Theorem 2.17.** *When  $\lambda = \lambda_p = 0$  in (1.3) and (2.16) respectively, the solutions to (1.3) and (2.16) are identical as long as both optimizations are equivalently initialized.*

*Proof.* Using (2.11) and (2.12),

$$(2.31) \quad \begin{aligned} x \text{ solves (1.3)} &\iff \sigma_i \langle x, v_i \rangle = \langle b, u_i \rangle \\ &\iff p(\sigma_i^2)^{\frac{1}{2}} \sigma_i \langle x, v_i \rangle = p(\sigma_i^2)^{\frac{1}{2}} \langle b, u_i \rangle \\ &\iff x \text{ solves (2.16)} \end{aligned} \quad \blacksquare$$

**3. MRI Experiments.** In the spirit of reproducible research, the data and code used to perform the following experiments can be found at:

<https://github.com/sidward/ppcs><sup>1</sup>

All reconstructions were implemented in the Python programming language using SigPy<sup>2</sup> [35]. The polynomial optimizations (2.8) were performed using SymPy<sup>3</sup> [30], with the latter lever-

<sup>1</sup><https://doi.org/10.5281/zenodo.6475880>

<sup>2</sup><https://doi.org/10.5281/zenodo.5893788>

<sup>3</sup><https://doi.org/10.7717/peerj-cs.103>

aging an excellent Chebyshev polynomial package available at <https://github.com/mlazarc/Chebyshev><sup>4</sup>.

To verify the efficacy of the preconditioner, three varied MRI reconstructions were studied using the unconstrained formulations (1.3) and (2.16). The Nesterov accelerated variants, Algorithm 2.2 and Algorithm 2.4, were used over their respective non-accelerated counterparts. For all cases, the corresponding measurement matrix  $A$  was normalized to have a unitary induced  $l_2$ -norm, and the measurement vector  $b$  was normalized to have unitary  $l_2$ -norm. All experiments were performed on an Intel (R) Xeon Gold 5320 CPU and NVIDIA(R) RTX A6000 GPUs.

**3.1. Parameter Selection.** Before discussing the specific experiments, this section will describe the efforts undertaken to ensure that each algorithm is portrayed in the best light.

Solving linear inverse problems posed as (1.3) and (2.16) using FISTA, IFISTA, ADMM and the proposed method requires the user to specify the regularization value (for each algorithm) and the desired number of  $A^*A$  evaluations per iteration (for each algorithm modulo FISTA). FISTA utilizes one  $A^*A$  evaluation per iteration. IFISTA and the proposed polynomial preconditioner, when using a polynomial  $d$ , utilizes  $(d+1)$   $A^*A$  evaluations per iteration. ADMM utilizing  $n$   $A^*A$  evaluations per iteration implies  $(n-1)$  conjugate gradient (CG) iterations during the inner loop of ADMM (as one  $A^*A$  evaluation is needed to calculate the initial residual term in the CG algorithm). IFISTA and the proposed method require additional tuning of the regularization value as argued by the introduction of  $\lambda_p$  in (2.16).

The convergence of the iterates of the respective algorithms and the quality of the converged result are dependent on the regularization value chosen and the number of  $A^*A$  evaluations per iteration. A fair comparison between the algorithms necessitates a search through the large parameter space of regularization values and the number of normal evaluations. It is difficult to manually choose parameters based on the observed convergence and reconstruction quality. To overcome this, the following programmatic procedure is used to select the parameters.

1. For all algorithms, the maximum number of total  $A^*A$  evaluations is fixed.
2. The minimum normalized root mean squared error (NRMSE) achieved by FISTA (with respect to the reference image) among all tested regularization values ( $\lambda$ ) is noted as  $\epsilon_f$  %.
3. For each method, if a parameter set yields a reconstruction with NRMSE (with respect to the reference image) that is greater than  $(\epsilon_f + 2)$ %, then that parameter set is discarded. The “+2” term was set to account for the finite resolution of the grid search of regularization values ( $\lambda$ ) and potential numerical errors. This “+2” term was observed to yield qualitatively similar reconstruction to the minimum NRMSE FISTA result for each of the following experiments. Note that the reconstruction error achieved might be lower than  $\epsilon_f$  %.
4. For each method, the convergence curves (with respect to the last iterate) as a function of the observed wall-time is calculated for the remaining parameter sets that satisfy the  $(\epsilon_f + 2)$ % constraint.
5. A log-linear fitting of the convergence curves is performed, and the parameters with

---

<sup>4</sup><https://doi.org/10.5281/zenodo.5831845>

the most negative slope (after the log-linear fitting) is chosen to represent the method.

By selecting parameters that yield reconstructions that fall within  $(\epsilon_f + 2)\%$  NRMSE of the reference, the reconstruction quality is assured. Given the subset of parameters, the convergence is calculated with respect to the last iterate of the respective methods instead of the reference image to directly show-case iterative convergence, which allows the resulting plots in the following experiments to be directly interpreted in the context of (2.7) and (2.21).

Please see Subsection 3.2 for a visual example of the parameter selection process proposed in this section.

**3.2. Cartesian MRI.** The first experiment is a 2D-Cartesian Compressed Sensing Knee application using publicly available data [34, 43]. The reference data was acquired using a 3D-FSE CUBE acquisition with proton density weighting that included fat saturation[43] on a 3T whole-body scanner (GE Healthcare, Waukesha, WI) using an 8-channel HD knee coil (GE Healthcare, Milwaukee, WI,USA) with an echo time (TE) of 25ms and repetition time (TR) of 1550ms. The field-of-view was 160mm, the matrix size was  $320 \times 320$ , slice thickness was 0.6mm and 256 slices were acquired. The reference data was fully-sampled and satisfied the Nyquist criterion. This reference data was retrospectively under-sampled by approximately  $R = 7.21$  times using a variable density Poisson disc sampling mask generated by BART[49].

The unconstrained reconstruction formulation (1.3) for this experiment is as follows:

$$(3.1) \quad x^* = \left\{ \underset{x}{\operatorname{argmin}} \frac{1}{2} \|MFSx - b\|_2^2 + \lambda \|Wx\|_1 \right.$$

Here,  $W$  is the forward Daubechies-4 Wavelet transform,  $S$  is the SENSE model of the parallel-imaging acquisition [41] estimated using [48],  $F$  is the 2D-Fourier transform and  $M$  is the Poisson disc sampling mask.

This application was solved with FISTA, IFISTA, ADMM and FISTA with the polynomial preconditioner. Each algorithm was allowed to run for a maximum of 60  $A^*A$  evaluations. For FISTA, IFISTA and polynomial preconditioned FISTA, regularization values  $\lambda$  were varied as:

$$(3.2) \quad \lambda \in \left\{ \frac{10^{-2}}{1.5^k} : k = 0, 1, \dots, 14 \right\}$$

For IFISTA, ADMM and the polynomial preconditioned FISTA, the number of  $A^*A$  evaluations were varied as:

$$(3.3) \quad A^*A \text{ evaluations per iteration} \in \{2, 3, 4, 5, 6\}$$

The number of  $A^*A$  evaluations per iteration were chosen to cleanly divide the maximum number of  $A^*A$  evaluations for fair comparison between methods. Lastly, the regularization value from the FISTA experiments with the least NRMSE against the reference image was used for ADMM, with the step size ( $\rho$ ) varied as:

$$(3.4) \quad \rho \in \left\{ 3^k : k = -7, -6, \dots, -1, 0, 1, \dots, 6, 7 \right\}$$

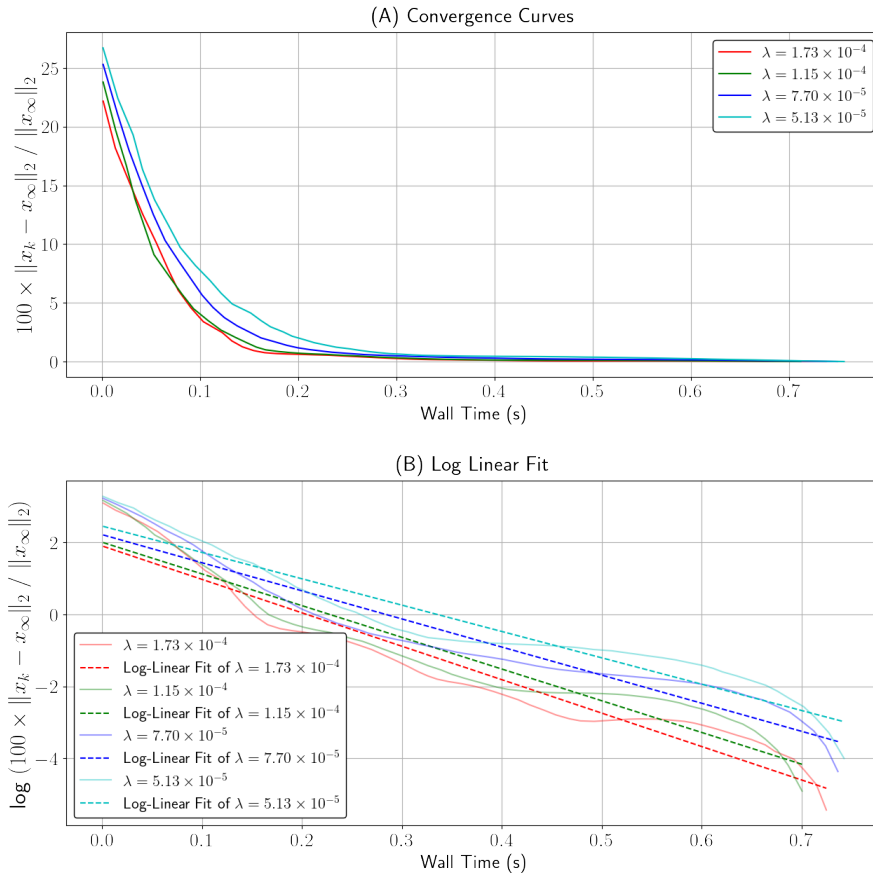


**Figure 2. Parameter Selection.** This figure demonstrates how the hyper-parameters were chosen to represent FISTA. Among the hyper-parameters tested in (3.2), the minimum NRMSE against the reference image achieved by FISTA was  $\epsilon_f = 13.61\%$ . The four  $\lambda$  values shown in (A) and (B) achieved  $(\epsilon_f + 2)\%$  NRMSE. In order to programmatically pick the fastest converging value between the listed four values, a log-linear fitting of the convergence curves is performed, as shown in (B). The parameter with the most negative log-linear slope is chosen to represent the algorithm, which in this case is the  $\lambda = 1.73 \times 10^{-4}$  curve.

To give a visual example of how the programmatic selection works (Subsection 3.1), among the  $\lambda$  values tested in (3.2), the minimum NRMSE achieved by FISTA was  $\epsilon_f = 13.61\%$ . It is observed that for FISTA, four different regularization values  $\lambda$  achieved  $(\epsilon_f + 2)\%$  or less NRMSE with respect to the reference image. Qualitatively, the  $\lambda = 1.73 \times 10^{-4}$  curve achieved the fastest iterative convergence as shown in Figure 2(A). This is seen to translate to the most negative slope for the corresponding log-linear fit as shown in Figure 2(B) and is thus the parametric value chosen to represent FISTA.

For IFISTA, ADMM and the proposed method, the identical process was used (with the same  $(\epsilon_f + 2)\%$  NRMSE condition) to choose representative regularization value and number of  $A^*A$  evaluations per iteration.

The convergence curves of the respective methods after the programmatically chosen parameters with respect to both, the number of  $A^*A$  evaluations and observed wall times, are

depicted in Figure 3, and the final iterates of the corresponding methods are depicted in Figure 6 along with the sampling mask  $M$  leveraged in (3.1).

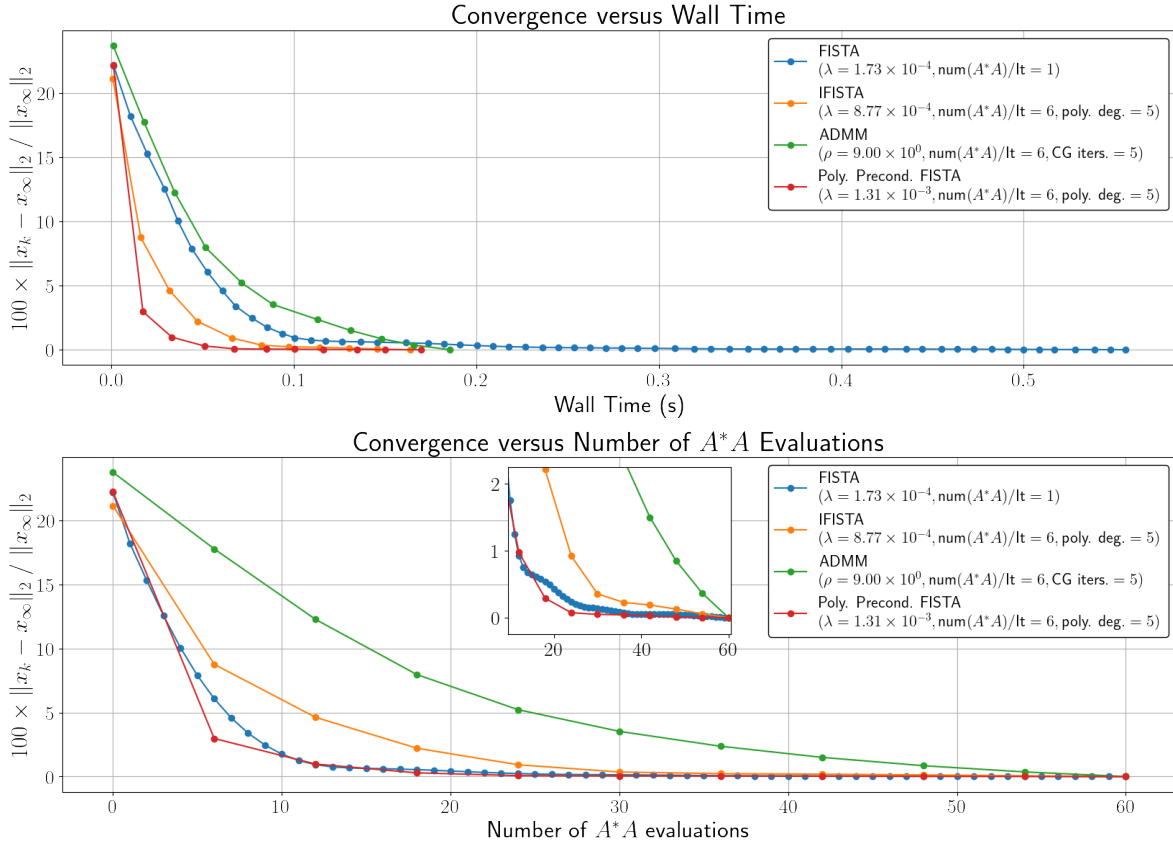


**Figure 3. Cartesian MRI Convergence Results.** This figure depicts the convergence results of the respective methods described in Subsection 3.2 given the hyper-parameters selected as in Subsection 3.1 with  $\epsilon_f = 13.61\%$ . Given the chosen hyper-parameters, the error over iterations with respect to the last iteration of each respective method is plotted. The  $k^{\text{th}}$  iteration and last iteration are labelled as  $x_k$  and  $x_\infty$  respectively. The legend on the top right depicts the algorithm and the chosen hyper-parameters. The x-axis of the top and bottom subplots denotes the total number of  $A^*A$  evaluations and measured wall-times respectively. The circular-markings on each line denote the respective iteration points. The number of proximal operators evaluated by a point on the x-axis is equal to the number of iterations by that point.

**3.3. Non-Cartesian MRI.** The second experiment is a 2D non-Cartesian variable-density spiral brain application using data that is publicly available at the code repository<sup>5</sup>. Reference data was acquired on a 3T scanner (GE Healthcare, Waukesha, WI) with IRB approval and informed consent obtained using 32 coils with a variable density spiral trajectory at  $1\text{mm} \times 1\text{mm}$  resolution and a field-of-view of  $220\text{mm} \times 220\text{mm}$ . The trajectory was designed with 16-fold in-plane under-sampling at the center of k-space and a linearly increasing under-sampling

<sup>5</sup><https://github.com/sidward/ppcs>



rate up to 32-fold at the edge of k-space. The readout duration was 6.7ms. This reference data was SVD coil-compressed to 12 coils, and then retrospectively under-sampled by discarding every other interleaves out of 32 interleaves.

The unconstrained reconstruction formulation (1.3) for this experiment is as follows:

$$(3.5) \quad x^* = \underset{x}{\operatorname{argmin}} \frac{1}{2} \|\mathcal{F}Sx - b\|_2^2 + \lambda \|Wx\|_1$$

Here,  $W$  is the forward Daubechies-4 Wavelet transform,  $S$  is the SENSE model of the parallel-imaging acquisition [41] estimated using [48], and  $\mathcal{F}$  is the non-uniform Fourier transform. This experiment utilized the Toeplitz structure of  $\mathcal{F}^*\mathcal{F}$  for faster evaluation for both (1.3) and (2.16)[53, 14, 1].

This application was solved with FISTA, IFISTA, ADMM and FISTA with the polynomial preconditioner. The regularization values  $(\lambda, \rho)$  tested were the same as in Subsection 3.2. The maximum number of  $A^*A$  set to 80. For IFISTA, ADMM and the polynomial preconditioned FISTA, the number of  $A^*A$  evaluations were varied as:

$$(3.6) \quad A^*A \text{ evaluations per iteration} \in \{2, 4, 5, 8, 10\}$$

The number of  $A^*A$  evaluations per iteration were chosen to cleanly divide the maximum number of  $A^*A$  evaluations for fair comparison between methods.

The same programmatic procedure as in Subsection 3.1 was used to select representative parameters for each method with the best FISTA reconstruction achieving an NRMSE of  $\epsilon_f = 16.03\%$ . The convergence curves of the respective methods after the programmatically chosen parameters with respect to both, the number of  $A^*A$  evaluations and observed wall times, are depicted in Figure 4, and the final iterates of the corresponding methods are depicted in Figure 7. Figure 9 shows the utilized trajectory in (3.5).

**3.4. Spatio-Temporal MRI.** The third experiment is a 3D non-Cartesian spatio-temporal brain application. The data were obtained on a 3T scanner (GE Healthcare, Waukesha, WI) with IRB approval and informed consent obtained. The reference data were acquired with 48 channel coils using a 3D MRF [28] acquisition with the TGAS-SPI trajectory with a total of 48 groups acquired to achieve adequate 3D k-space encoding at each temporal data point [6].

Each acquisition group contains an adiabatic inversion preparation with TI of 15ms and 500 variable flip-angle acquisitions with TR of 12.5 ms and TE of 1.75ms, with a 1.2s wait time for signal recovery to improve the signal-to-noise ratio, resulting in a net acquisition per group of 7.45s and total acquisition time of approximately 6 minutes. Additionally, a water-exciting rectangular pulse with duration of 2.38ms was used to depress the fat signal [33]. A variable density spiral trajectory with a 16-fold in-plane under-sampling rate at the center of k-space and a 32-fold under-sampling rate at the edge of k-space was used to achieve an encoding at 1-mm isotropic resolution with a field-of-view of  $220 \times 220 \times 220 \text{ mm}^3$  with a readout duration of 6.7 ms. This reference data was coil-compressed to 10 coils (from 48) using a combination of [22] and SVD coil compression. Retrospective under-sampling was performed to simulate a 1 minute acquisition. The data used is publicly available at the code repository<sup>6</sup>.

---

<sup>6</sup><https://github.com/sidward/ppcs>

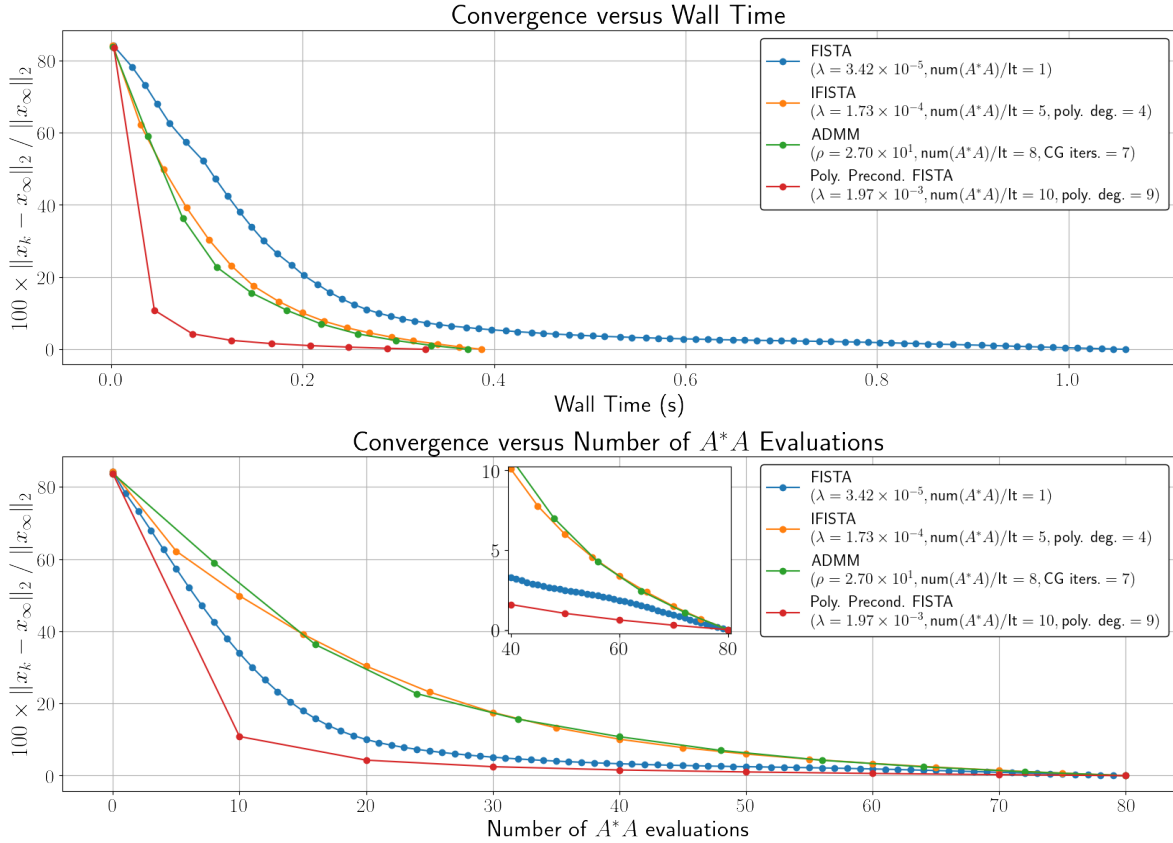


**Figure 4. Non-Cartesian MRI Convergence Results.** This figure depicts the convergence results of the respective methods described in Subsection 3.3 given the hyper-parameters selected as in Subsection 3.1 with  $\epsilon_f = 16.03\%$ . Given the chosen hyper-parameters, the error over iterations with respect to the last iteration of each respective method is plotted. The  $k^{\text{th}}$  iteration and last iteration are labeled as  $x_k$  and  $x_\infty$  respectively. The legend on the top right depicts the algorithm and the chosen hyper-parameters. The x-axis of the top and bottom subplots denotes the total number of  $A^*A$  evaluations and measured wall-times respectively. The circular-markings on each line denote the respective iteration points. The number of proximal operators evaluated by a point on the x-axis is equal to the number of iterations by that point.

The unconstrained reconstruction formulation (1.3) for this experiment is as follows [24, 38, 29, 59, 46, 6]:

$$(3.7) \quad x^* = \left\{ \underset{x}{\operatorname{argmin}} \frac{1}{2} \|D^{1/2} (\mathcal{F}S\Phi x - b)\|_2^2 + \lambda \text{LLR}(x) \right.$$

Here, LLR is the locally-low rank constraint [46] with a block-size of  $8 \times 8 \times 8$ ,  $S$  is the SENSE model of the parallel-imaging acquisition [41] estimated using [57] and  $\mathcal{F}$  is the 3D non-uniform Fourier transform. Note that in this case, the reconstructed  $x$  consists of multiple “coefficient” images such that  $\Phi x$  recovers the temporal evolution of the underlying signal. Please see [24, 28, 46, 6, 54, 17, 58, 52, 3, 51] for more information. (3.7) leverages structural

left-preconditioning  $D$  for faster convergence. The particular method used to derive  $D$  was [39]. Since the structural left-preconditioner ( $D$ ) derived from [39] differs between the 6-minute acquisition and 1-minute acquisition, the 1-minute FISTA reconstruction of the data is used as a reference for fair comparison.

The inclusion of  $D$  reduces the theoretical efficacy of the polynomial preconditioner as the resulting normal operator when solving (3.7) (i.e.  $A^*DA$ ) has a much narrower eigenvalue spectrum compared to  $A^*A$ . That being said, utilizing the polynomial preconditioner (which can be directly applied to (3.7) thanks to its generalizability) can still be beneficial to reduce real world reconstruction times. In particular, given the same number of  $A^*A$  evaluations, the polynomial preconditioner achieves qualitatively similar reconstruction to the non polynomial preconditioned result while utilizing fewer proximal calls. For applications where evaluating  $A^*A$  is much faster than a proximal call (such as in the sequel), the fewer proximal evaluations yields significant reductions in processing times.

For this TGAS-SPI-MRF application, (3.7) is too big to solve directly on even high-end GPUs without utilizing some form of “batching” that moves data between CPU memory and GPU memory when evaluating matrix-vector products of  $A$  and  $A^*$ . This increases the per-iteration costs. Instead, an ADMM formulation is leveraged to split (3.7) into smaller sub problems, where each sub problem completely fits (that is to say, there is no need to implement any kind of batching) in approximately 20GB of GPU memory. Each sub problem can then be solved in parallel on separate GPU devices with significantly fewer data transfers between CPU and GPU devices.

The sequel uses 3 GPU devices, but the available code<sup>7</sup> generalizes to the number of available GPUs. Let  $(A_1, b_1)$  denote the forward model and acquired data of the first three (of ten) receiver channels,  $(A_2, b_2)$  denote the next three, and  $(A_3, b_3)$  denote the following three. The last coil is discarded for now so that each device processes an equal number of channel data, but future work will be to explore better ways to integrate all available coils when the number of GPU devices do not cleanly divide the number of coils.

Sub problems  $f_1, f_2$  and  $f_3$  are then defined as:

$$(3.8) \quad \begin{aligned} f_i &= \frac{1}{2}\|A_i x - b_i\|_2^2 + \frac{\lambda}{3}LLR(x) \\ &\text{for } i \in \{1, 2, 3\} \end{aligned}$$

Note that the sum of the sub problems, i.e.  $f_1 + f_2 + f_3$ , equals the objective of (3.7). This can now be solved using Global Consensus ADMM [37], listed as Algorithm 3.1.

With  $\{f_i\}$  as the sub problems, Algorithm 3.1 can be used to solve (3.7). (3.9a) and (3.9c) can be evaluated independently of each other in parallel on separate devices, with data movement between CPU and GPU occurring only during (3.9b). (3.9a) yields a regularized linear inverse problem similar to (3.7), and can thus be solved with FISTA and the polynomial preconditioner. When solving this sub problem,  $A_i$  is much faster to evaluate compared to the proximal operator of the LLR regularization, making the proximal evaluation the bottleneck. Utilizing polynomial preconditioning allows for similar quality reconstruction given the same number of  $A^*A$  evaluations but with fewer proximal calls, resulting in faster processing times.

---

<sup>7</sup><https://github.com/sidward/ppcs>

**Algorithm 3.1** Global Consensus ADMM [37]*Inputs:*

- Sub problems  $\{f_1, f_2, \dots, f_N\}$
- ADMM step-size  $\rho$
- $\bar{x} = 0$
- $x^i = 0$
- $u^i = 0$

*Step k:* ( $k \geq 0$ ) Compute

$$(3.9a) \quad x_{k+1}^i = \mathbf{prox}_{\rho f_i}(\bar{x}_k - u_k^i)$$

$$(3.9b) \quad \bar{x}_{k+1} = \frac{1}{N} \sum_i x_{k+1}^i$$

$$(3.9c) \quad u_{k+1}^i = u_k^i + x_{k+1}^i - \bar{x}_{k+1}^i$$

Given the size of the problem, the following experiment only considers FISTA with and without the proposed preconditioner. The maximum number of normal evaluations was set to 40. The ADMM step size was set to  $1 \times 10^3$ . For both, the standard FISTA and the polynomial preconditioned FISTA implementations of (3.9a), the respective  $\lambda$  and  $\lambda_p$  values were qualitatively tuned for the best reconstruction performance. The respective convergence curves when solving sub problem associated with  $f_1$  during the first ADMM iteration is depicted in Figure 5, and the final reconstruction after 2 ADMM iterations are depicted in Figure 8. The polynomial preconditioning resulted in an approximately  $2 \times$  faster reconstruction.

With respect to real word performance, the synchronization step (3.9b) took approximately 26 seconds. Thus the polynomial preconditioned reconstructions depicted in Figure 8 where achieved in just over 10 minutes.

**4. Discussion.** The polynomial preconditioner is seen to improve the conditioning of the unconstrained formulation (1.3), resulting in faster convergence compared to standard FISTA, IFISTA and ADMM. With appropriate tuning of  $\lambda_p$  in (2.16), the reconstructed images with the preconditioner are qualitatively similar to the solutions of (1.3).

By utilizing the permutability provided by polynomials and linear operators, the polynomial preconditioner is applied to the iterates directly instead of in the range space of  $A$ , thus significantly reducing the computational requirements (assuming  $n$  is much smaller than  $m$ , which is often the case in computational MRI). Consequently, none of the preconditioned unconstrained reconstructions utilized any dual variables or an application-specific preconditioner array, resulting in comparable computational memory requirements to FISTA. Additionally, it enables the use of the faster  $A^*A$  evaluations if applicable, such as in Subsection 3.3, which is not possible with [36].

While the proposed preconditioner does increase the per-iteration computational cost com-

pared to FISTA, the proposed method enables faster computation compared to FISTA even when requiring that both methods to utilize an equal number of  $A^*A$  evaluations. This is because, on-top of the theoretically faster convergence offered by the polynomial preconditioner (as verified by the convergence curve as a function of the number of  $A^*A$  evaluations), utilizing the preconditioner enables fewer proximal operator evaluations while still achieving comparable reconstruction. In particular, for the experiments showcased in this manuscript, the proximal operator is more computational expensive compared to evaluating  $A^*A$ , translating to significantly faster real-world performance as demonstrated by the convergence curve versus wall-time, while achieving similar reconstruction performance. The reduced number of proximal evaluations of the proposed method will be of even more benefit for highly intensive proximal operators, such as the structured matrix completion approaches akin to the soft-thresholding versions of [16, 45].

The generalizability of the polynomial preconditioner allows it to be used directly in a subspace-reconstruction [24, 38, 29, 59, 46, 6] without needing to explicitly account for  $\Phi$  when designing the preconditioner while also easily integrating the structure-specific left-preconditioning ( $D$  in (3.7)). By utilizing  $A^*A$  to construct the preconditioner, the method inherently takes into account information from  $\Phi, S, \mathcal{F}$  and  $\mathcal{D}$  without user modification. In particular, as depicted in Figure 8, the combination of  $\mathcal{D}$ , the ADMM parallel processing and the polynomial preconditioner enabled a high quality reconstruction in just over 10 minutes, which is an approximately  $12\times$  improvement over the computation times reported in [6].

Looking at the convergence of iterates as a function of the number of  $A^*A$  evaluations, IFISTA performs slightly worse than standard FISTA in Subsection 3.2 and Subsection 3.3. This is arguably because, as discussed in Subsection 2.7, the IFISTA preconditioner cannot be pre-calculated and is instead evaluated in a matrix-free manner. In contrast, by explicitly optimizing for the faster convergence of iterates for a given degree via (2.8), the proposed polynomial preconditioner enables faster convergence.

This work does not explore incorporating a weighting-prior into the spectral cost ( $w$  in (2.22)). It is expected that a reasonable prior estimate of the spectrum of an operator  $A$  derived for a specific application will significantly improve the rate of convergence for that application. However, given the large dimensionality of  $A$  and the consequent difficulty in approximating the spectrum of  $A^*A$ , estimating a reasonable prior  $w$  will involve trial-and-error, and is thus left to future work.

A limitation of the polynomial preconditioner is with respect to numerical stability. In principle, it is possible to utilize a polynomial  $p$  of a high degree  $d$ . However, in practice, evaluating powers of  $A^*A$  can accumulate numerical errors. Therefore, tuning the degree  $d$  for the application of interest is required.

The error bound presented in Theorem 2.15 is applicable to any linear operator  $P$  such that  $P$  is injective on  $\text{null}(A)^\perp$ . Thus, deriving a  $P$  to minimize the error bound in (2.26) is a promising avenue for application-specific preconditioner design. For example, (2.26) can be used to upper-bound the error of the circulant preconditioner in [31].

**Acknowledgments.** The authors would like to thank Dr. Sophie Schauman for testing the reproducibility code, Dr. Martin Uecker for providing additional references and Dr. Tao Hong for the IFISTA reference.

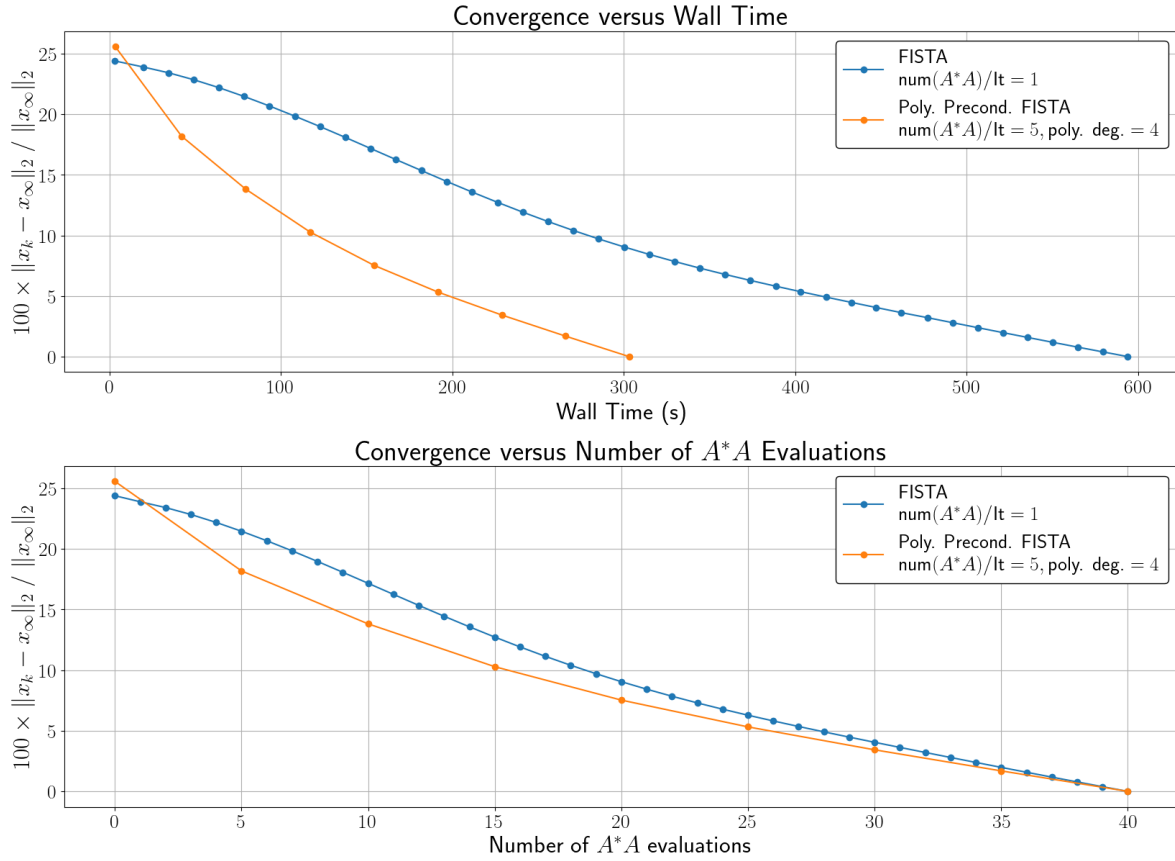


**Figure 5. Spatio-Temporal MRI Convergence Results.** This figure depicts the convergence results of evaluating (3.9a) for the first sub problem  $f_1$ . Given the chosen hyper-parameters, the error over iterations with respect to the last iteration of each respective method is plotted. The  $k^{\text{th}}$  iteration and last iteration are labelled as  $x_k$  and  $x_\infty$  respectively. The legend on the top right depicts the algorithm and the chosen hyper-parameters. The x-axis of the top and bottom subplots denotes the total number of  $A^*A$  evaluations and measured wall-times respectively. The circular-markings on each line denote the respective iteration points. The number of proximal operators evaluated by a point on the x-axis is equal to the number of iterations by that point.

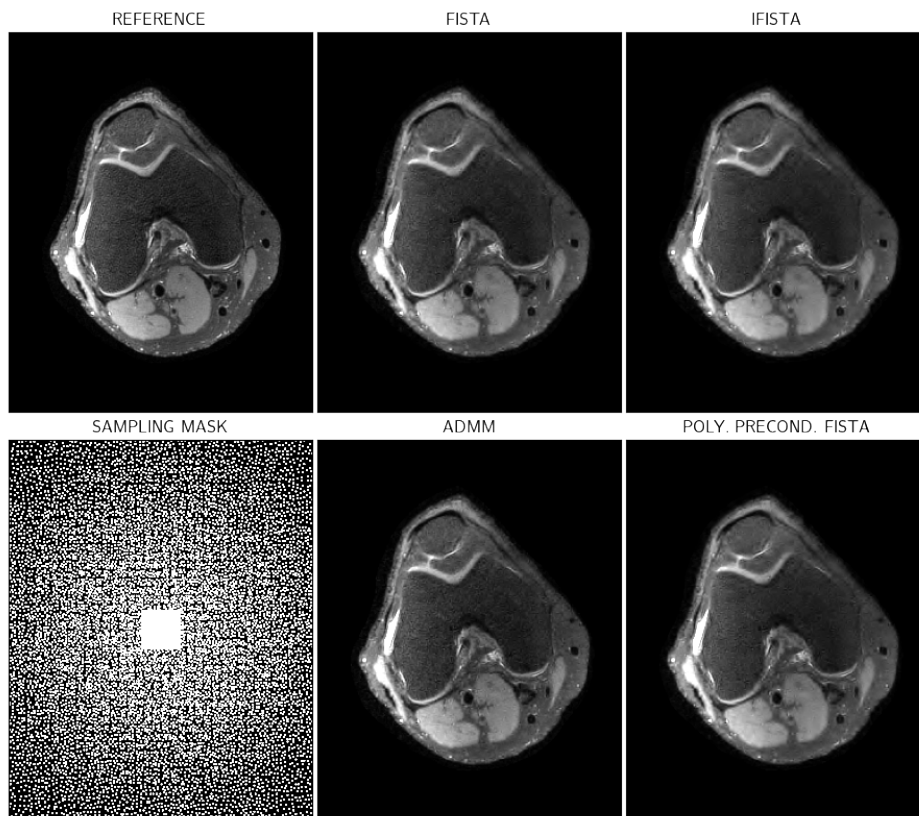


**Figure 6.** *Cartesian MRI Reconstruction Results.* This figure depicts the final iterations of the respective methods in Figure 3. The bottom left figure, labelled “SAMPLING MASK”, denotes the under-sampling mask used in (3.1). The hyper-parameters for these results are depicted in Figure 3.

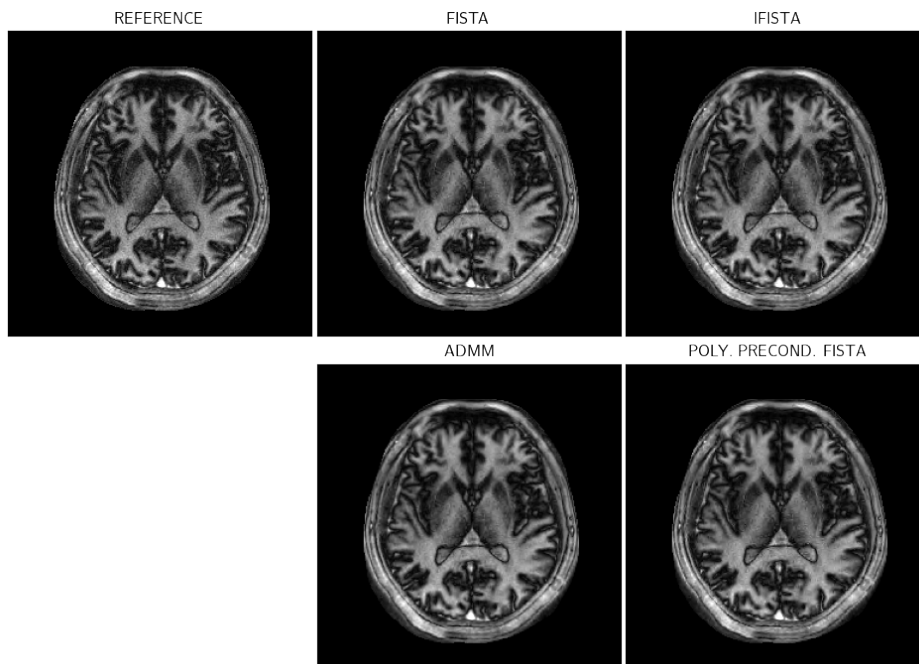


**Figure 7.** *Non-Cartesian MRI Reconstruction Results.* This figure depicts the final iterations of the respective methods in Figure 4. The hyper-parameters for these results are depicted in Figure 4.

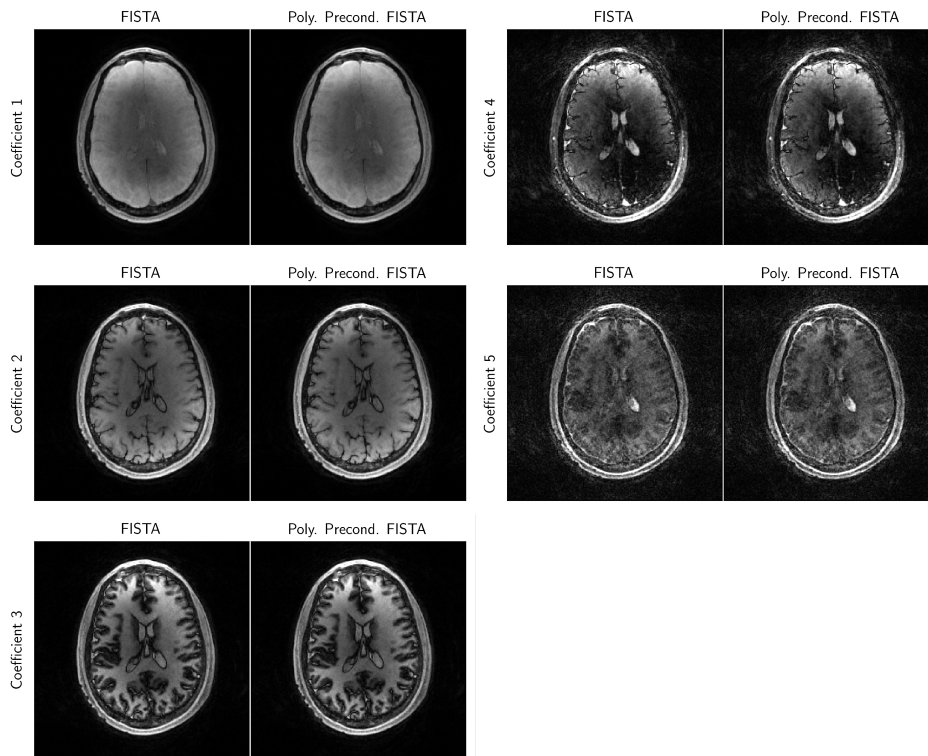


**Figure 8.** *Spatio-Temporal MRI Reconstruction Results.* This figure depicts the reconstructions after two ADMM iterations, where (3.9a) is evaluated using (left) FISTA and (right) Polynomial Preconditioned FISTA. The hyper-parameters for these results are depicted in Figure 5.



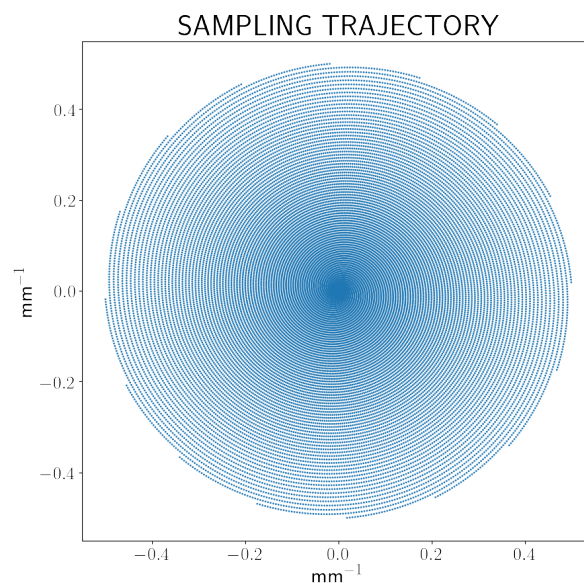


**Figure 9.** *Non-Cartesian MRI Trajectory.* This figure depicts the under-sampled trajectory used in (3.5).

## REFERENCES

- [1] C. BARON, N. DWORK, J. M. PAULY, AND D. NISHIMURA, *Rapid compressed sensing reconstruction of 3D non-Cartesian MRI*, *Magnetic Resonance in Medicine*, 79 (2018), pp. 2685–2692.
- [2] A. BECK AND M. TEOULLE, *A fast iterative shrinkage-thresholding algorithm for linear inverse problems*, *SIAM Journal on Imaging Sciences*, 2 (2009), pp. 183–202.
- [3] N. BEN-ELIEZER, D. K. SODICKSON, AND K. T. BLOCK, *Rapid and Accurate T2 Mapping from Multi-spin-echo Data using Bloch-simulation-based Reconstruction*, *Magnetic Resonance in Medicine*, 73 (2015), pp. 809–817.
- [4] K. T. BLOCK, M. UECKER, AND J. FRAHM, *Undersampled Radial MRI with Multiple Coils. Iterative Image Reconstruction Using a Total Variation Constraint*, *Magnetic Resonance in Medicine*, 57 (2007), pp. 1086–1098.
- [5] P. CAO, X. ZHU, S. TANG, A. LEYNES, A. JAKARY, AND P. E. LARSON, *Shuffled Magnetization-prepared Multicontrast Rapid Gradient-echo Imaging*, *Magnetic Resonance in Medicine*, 79 (2018), pp. 62–70.
- [6] X. CAO, C. LIAO, S. S. IYER, Z. WANG, Z. ZHOU, E. DAI, G. LIBERMAN, Z. DONG, T. GONG, H. HE, J. ZHONG, B. BILGIC, AND K. SETSOMPOP, *Optimized multi-axis spiral projection mr fingerprinting with subspace reconstruction for rapid whole-brain high-isotropic-resolution quantitative imaging*, *Magnetic Resonance in Medicine*, 88 (2022), pp. 133–150, <https://doi.org/https://doi.org/10.1002/mrm.29194>, <https://onlinelibrary.wiley.com/doi/abs/10.1002/mrm.29194>.
- [7] A. CHAMBOLLE AND C. DOSSAL, *On the Convergence of the Iterates of the “Fast Iterative Shrinkage/Thresholding Algorithm”*, *Journal of Optimization Theory and Applications*, 166 (2015), pp. 968–982.
- [8] A. CHAMBOLLE AND T. POCK, *A First-Order Primal-Dual Algorithm for Convex Problems with Applications to Imaging*, *Journal of Mathematical Imaging and Vision*, 40 (2011), pp. 120–145.
- [9] C. CHEN, L. HE, H. LI, AND J. HUANG, *Fast iteratively reweighted least squares algorithms for analysis-based sparse reconstruction*, *Medical Image Analysis*, 49 (2018), pp. 141–152.
- [10] S. S. CHEN, D. L. DONOHO, AND M. A. SAUNDERS, *Atomic decomposition by basis pursuit*, *SIAM Review*, 43 (2001), pp. 129–159.

- [11] I. DAUBECHIES, R. DEVORE, M. FORNASIER, AND C. S. GÜNTÜRK, *Iteratively reweighted least squares minimization for sparse recovery*, Communications on Pure and Applied Mathematics, 63 (2010), pp. 1–38, <https://doi.org/https://doi.org/10.1002/cpa.20303>, <https://onlinelibrary.wiley.com/doi/abs/10.1002/cpa.20303>, <https://arxiv.org/abs/https://onlinelibrary.wiley.com/doi/pdf/10.1002/cpa.20303>.
- [12] J. A. FESSLER, *Michigan image reconstruction toolbox*, <https://github.com/JeffFessler/MIRT.jl>.
- [13] J. A. FESSLER, *Optimization methods for magnetic resonance image reconstruction: Key models and optimization algorithms*, IEEE Signal Processing Magazine, 37 (2020), pp. 33–40.
- [14] J. A. FESSLER, S. LEE, V. T. OLAFSSON, H. R. SHI, AND D. C. NOLL, *Toeplitz-based iterative image reconstruction for mri with correction for magnetic field inhomogeneity*, IEEE Transactions on Signal Processing, 53 (2005), pp. 3393–3402.
- [15] S. FOUCAIT AND H. RAUHUT, *A Mathematical Introduction to Compressive Sensing*, Springer New York, 2013, [https://doi.org/10.1007/978-0-8176-4948-7\\_1](https://doi.org/10.1007/978-0-8176-4948-7_1).
- [16] J. P. HALDAR, *Low-rank modeling of local k-space neighborhoods (loraks) for constrained mri*, IEEE Transactions on Medical Imaging, 33 (2013), pp. 668–681.
- [17] C. HUANG, A. BILGIN, T. BARR, AND M. I. ALTBACH, *T2 Relaxometry with Indirect Echo Compensation from Highly Undersampled Data*, Magnetic Resonance in Medicine, 70 (2013), pp. 1026–1037, <https://doi.org/10.1002/mrm.24540>, <https://onlinelibrary.wiley.com/doi/abs/10.1002/mrm.24540>, <https://arxiv.org/abs/https://onlinelibrary.wiley.com/doi/pdf/10.1002/mrm.24540>.
- [18] S. IYER, F. ONG, AND K. SETSOMPOP, *Polynomial Preconditioning for Accelerated Convergence of Proximal Algorithms including FISTA*, Proceedings of the International Society of Magnetic Resonance in Medicine, London, United Kingdom, (2022).
- [19] O. G. JOHNSON, C. A. MICCHELLI, AND G. PAUL, *Polynomial Preconditioners for Conjugate Gradient Calculations*, SIAM Journal on Numerical Analysis, 20 (1983), pp. 362–376.
- [20] S. KANIEL, *Estimates for Some Computational Techniques in Linear Algebra*, Mathematics of Computation, 20 (1966), pp. 369–378.
- [21] S. KECSKEMETI, A. SAMSONOV, S. A. HURLEY, D. C. DEAN, A. FIELD, AND A. L. ALEXANDER, *MPnRAGE: A Technique to Simultaneously Acquire Hundreds of Differently Contrasted MPRAGE Images with Applications to Quantitative T1 Mapping*, Magnetic Resonance in Medicine, 75 (2016), pp. 1040–1053.
- [22] D. KIM, S. F. CAULEY, K. S. NAYAK, R. M. LEAHY, AND J. P. HALDAR, *Region-optimized virtual (rovir) coils: Localization and/or suppression of spatial regions using sensor-domain beamforming*, Magnetic Resonance in Medicine, 86 (2021), pp. 197–212, <https://doi.org/https://doi.org/10.1002/mrm.28706>, <https://onlinelibrary.wiley.com/doi/abs/10.1002/mrm.28706>, <https://arxiv.org/abs/https://onlinelibrary.wiley.com/doi/pdf/10.1002/mrm.28706>.
- [23] K. KOOLSTRA, J. VAN GEMERT, P. BÖRNERT, A. WEBB, AND R. REMIS, *Accelerating compressed sensing in parallel imaging reconstructions using an efficient circulant preconditioner for cartesian trajectories*, Magnetic Resonance in Medicine, 81 (2019), pp. 670–685, <https://doi.org/https://doi.org/10.1002/mrm.27371>.
- [24] Z.-P. LIANG, *Spatiotemporal imaging with partially separable functions*, in 2007 4th IEEE International Symposium on Biomedical Imaging, 2007 4th IEEE International Symposium on Biomedical Imaging: From Nano to Macro - Proceedings, 2007, pp. 988–991.
- [25] B. LIU, K. KING, M. STECKNER, J. XIE, J. SHENG, AND L. YING, *Regularized Sensitivity Encoding (SENSE) Reconstruction Using Bregman Iterations*, Magnetic Resonance in Medicine, 61 (2009), pp. 145–152.
- [26] M. LUSTIG, D. DONOHO, AND J. M. PAULY, *Sparse MRI: The application of compressed sensing for rapid MR imaging*, Magnetic Resonance in Medicine, 58 (2007), pp. 1182–1195, <https://doi.org/https://doi.org/10.1002/mrm.21391>.
- [27] M. LUSTIG, D. L. DONOHO, J. M. SANTOS, AND J. M. PAULY, *Compressed Sensing MRI*, IEEE Signal Processing Magazine, 25 (2008), pp. 72–82, <https://doi.org/10.1109/MSP.2007.914728>.
- [28] D. MA, V. GULANI, N. SEIBERLICH, K. LIU, J. L. SUNSHINE, J. L. DUERK, AND M. A. GRISWOLD, *Magnetic Resonance Fingerprinting*, Nature, 495 (2013), pp. 187–192.
- [29] M. MANI, M. JACOB, V. MAGNOTTA, AND J. ZHONG, *Fast iterative algorithm for the reconstruction of multishot non-cartesian diffusion data*, Magnetic Resonance in Medicine, 74 (2015), pp. 1086–

- 1094, <https://doi.org/https://doi.org/10.1002/mrm.25486>, <https://onlinelibrary.wiley.com/doi/abs/10.1002/mrm.25486>.
- [30] A. MEURER, C. P. SMITH, M. PAPROCKI, O. ČERTÍK, S. B. KIRPICHEV, M. ROCKLIN, A. KUMAR, S. IVANOV, J. K. MOORE, S. SINGH, T. RATHNAYAKE, S. VIG, B. E. GRANGER, R. P. MULLER, F. BONAZZI, H. GUPTA, S. VATS, F. JOHANSSON, F. PEDREGOSA, M. J. CURRY, A. R. TERREL, V. ROUČKA, A. SABOO, I. FERNANDO, S. KULAL, R. CIMRMAN, AND A. SCOPATZ, *SymPy: Symbolic Computing in Python*, PeerJ Computer Science, 3 (2017), p. e103.
- [31] M. J. MUCKLEY, D. C. NOLL, AND J. A. FESSLER, *Fast, Iterative Sub-Sampled Spiral Reconstruction via Circulant Majorizers*, Proceedings of the International Society of Magnetic Resonance in Medicine, Singapore, (2016).
- [32] Y. NESTEROV, *Lectures on Convex Optimization*, vol. 137, Springer, 2018.
- [33] O. NORBECK, T. SPRENGER, E. AVVENTI, H. RYDÉN, A. KITS, J. BERGLUND, AND S. SKARE, *Optimizing 3D EPI for Rapid  $T_1$ -Weighted Imaging*, Magnetic Resonance in Medicine, 84 (2020), pp. 1441–1455.
- [34] F. ONG, S. AMIN, S. VASANAWALA, AND M. LUSTIG, *mridata.org: An open archive for sharing MRI raw data*, Proceedings of the International Society of Magnetic Resonance in Medicine, Paris, France, (2018).
- [35] F. ONG AND M. LUSTIG, *SigPy: A Python Package for High Performance Iterative Reconstruction*, Proceedings of the International Society of Magnetic Resonance in Medicine, Montréal, Canada, 4819 (2019).
- [36] F. ONG, M. UECKER, AND M. LUSTIG, *Accelerating Non-Cartesian MRI Reconstruction Convergence Using  $k$ -Space Preconditioning*, IEEE Transactions on Medical Imaging, 39 (2020), pp. 1646–1654, <https://doi.org/10.1109/TMI.2019.2954121>.
- [37] N. PARIKH AND S. BOYD, *Proximal algorithms*, Foundations and Trends in Optimization, 1 (2014), pp. 127–239.
- [38] F. H. PETZSCHNER, I. P. PONCE, M. BLAIMER, P. M. JAKOB, AND F. A. BREUER, *Fast MR Parameter Mapping using  $k$ -t Principal Component Analysis*, Magnetic Resonance in Medicine, 66 (2011), pp. 706–716.
- [39] J. G. PIPE AND P. MENON, *Sampling density compensation in MRI: Rationale and an iterative numerical solution*, Magnetic Resonance in Medicine, 41 (1999), pp. 179–186.
- [40] K. P. PRUESSMANN, M. WEIGER, P. BÖRNERT, AND P. BOESIGER, *Advances in sensitivity encoding with arbitrary  $k$ -space trajectories*, Magnetic Resonance in Medicine, 46 (2001), pp. 638–651, <https://doi.org/https://doi.org/10.1002/mrm.1241>.
- [41] K. P. PRUESSMANN, M. WEIGER, M. B. SCHEIDEGGER, AND P. BOESIGER, *SENSE: Sensitivity Encoding for Fast MRI*, Magnetic Resonance in Medicine, 42 (1999), pp. 952–962.
- [42] S. RAMANI AND J. A. FESSLER, *Parallel MR Image Reconstruction Using Augmented Lagrangian Methods*, IEEE Transactions on Medical Imaging, 30 (2011), pp. 694–706, <https://doi.org/10.1109/TMI.2010.2093536>.
- [43] A. M. SAWYER, M. LUSTIG, M. ALLEY, P. UECKER, P. VIRTUE, P. LAI, AND S. VASANAWALA, *Creation of fully sampled mr data repository for compressed sensing of the knee*, (2013).
- [44] J. R. SHEWCHUK, *An Introduction to the Conjugate Gradient Method Without the Agonizing Pain*, School of Computer Science, Carnegie Mellon University, 1994.
- [45] P. J. SHIN, P. E. LARSON, M. A. OHLIGER, M. ELAD, J. M. PAULY, D. B. VIGNERON, AND M. LUSTIG, *Calibrationless parallel imaging reconstruction based on structured low-rank matrix completion*, Magnetic Resonance in Medicine, 72 (2014), pp. 959–970.
- [46] J. I. TAMIR, M. UECKER, W. CHEN, P. LAI, M. T. ALLEY, S. S. VASANAWALA, AND M. LUSTIG,  *$T_2$ -Shuffling: Sharp, multicontrast, volumetric fast spin-echo imaging*, Magnetic Resonance in Medicine, 77 (2017), pp. 180–195.
- [47] R. TIBSHIRANI, *Regression shrinkage and selection via the LASSO*, Journal of the Royal Statistical Society: Series B (Methodological), 58 (1996), pp. 267–288.
- [48] M. UECKER, P. LAI, M. J. MURPHY, P. VIRTUE, M. ELAD, J. M. PAULY, S. S. VASANAWALA, AND M. LUSTIG, *ESPIRiT—An Eigenvalue Approach to Autocalibrating Parallel MRI: Where SENSE Meets GRAPPA*, Magnetic Resonance in Medicine, 71 (2014), pp. 990–1001.
- [49] M. UECKER, F. ONG, J. I. TAMIR, D. BAHRI, P. VIRTUE, J. Y. CHENG, T. ZHANG, AND M. LUSTIG, *Berkeley Advanced Reconstruction Toolbox*, Proceedings of the International Society of Magnetic Res-

- onance in Medicine, Toronto, Canada, 23 (2015).
- [50] A. VAN DER SLUIS AND H. A. VAN DER VORST, *The Rate of Convergence of Conjugate Gradients*, *Numerische Mathematik*, 48 (1986), pp. 543–560.
- [51] J. V. VELIKINA, A. L. ALEXANDER, AND A. SAMSONOV, *Accelerating MR Parameter Mapping using Sparsity-promoting Regularization in Parametric Dimension*, *Magnetic Resonance in Medicine*, 70 (2013), pp. 1263–1273.
- [52] J. V. VELIKINA AND A. A. SAMSONOV, *Reconstruction of Dynamic Image Series from Undersampled MRI Data using Data-driven Model Consistency Condition (MOCCO)*, *Magnetic Resonance in Medicine*, 74 (2015), pp. 1279–1290.
- [53] F. WAJER AND K. PRUESSMANN, *Major speedup of reconstruction for sensitivity encoding with arbitrary trajectories*, *Proceedings of the International Society of Magnetic Resonance in Medicine*, Toronto, Canada, (2001).
- [54] F. WANG, Z. DONG, T. G. REESE, B. BILGIC, M. KATHERINE MANHARD, J. CHEN, J. R. POLIMENI, L. L. WALD, AND K. SETSOMPOP, *Echo Planar Time-Resolved Imaging (EPTI)*, *Magnetic Resonance in Medicine*, 81 (2019), pp. 3599–3615.
- [55] D. S. WELLER, S. RAMANI, AND J. A. FESSLER, *Augmented Lagrangian with Variable Splitting for Faster Non-Cartesian  $L_1$ -SPIRiT MR Image Reconstruction*, *IEEE Transactions on Medical Imaging*, 33 (2014), pp. 351–361, <https://doi.org/10.1109/TMI.2013.2285046>.
- [56] Z. XU, S. WANG, Y. LI, F. ZHU, AND J. HUANG, *Prim: An efficient preconditioning iterative reweighted least squares method for parallel brain mri reconstruction*, *Neuroinformatics*, 16 (2018), pp. 425–430.
- [57] L. YING AND J. SHENG, *Joint Image Reconstruction and Sensitivity Estimation in SENSE (JSENSE)*, *Magnetic Resonance in Medicine*, 57 (2007), pp. 1196–1202.
- [58] B. ZHAO, W. LU, T. K. HITCHENS, F. LAM, C. HO, AND Z.-P. LIANG, *Accelerated MR Parameter Mapping with Low-rank and Sparsity Constraints*, *Magnetic Resonance in Medicine*, 74 (2015), pp. 489–498.
- [59] B. ZHAO, K. SETSOMPOP, E. ADALSTEINSSON, B. GAGOSKI, H. YE, D. MA, Y. JIANG, P. ELLEN GRANT, M. A. GRISWOLD, AND L. L. WALD, *Improved magnetic resonance fingerprinting reconstruction with low-rank and subspace modeling*, *Magnetic Resonance in Medicine*, 79 (2018), pp. 933–942, <https://doi.org/https://doi.org/10.1002/mrm.26701>, <https://onlinelibrary.wiley.com/doi/abs/10.1002/mrm.26701>, <https://arxiv.org/abs/https://onlinelibrary.wiley.com/doi/pdf/10.1002/mrm.26701>.
- [60] M. ZULFIQUAR ALI BHOTTO, M. O. AHMAD, AND M. N. S. SWAMY, *An improved fast iterative shrinkage thresholding algorithm for image deblurring*, *SIAM Journal on Imaging Sciences*, 8 (2015), pp. 1640–1657.